Check for updates

Iodine quantification in limited angle tomography

Koen Michielsen and Alejandro Rodríguez-Ruiz[†]
Department of Medical Imaging, Radboud University Medical Center, Nijmegen 6500 HB, The Netherlands

Ingrid Reiser
Department of Radiology, The University of Chicago, Chicago, IL 60637, USA

James G. Nagy
Department of Mathematics and Computer Science, Emory University, Atlanta, GA 30322, USA

Ioannis Sechopoulos[a)]
Department of Medical Imaging, Radboud University Medical Center, Nijmegen 6500 HB, The Netherlands
Dutch Expert Center for Screening (LRCB), Nijmegen 6538 SW, The Netherlands

(Received 4 May 2020; accepted for publication 6 July 2020;
published 16 August 2020)

Purpose: To develop and test the feasibility of a two-pass iterative reconstruction algorithm with material decomposition designed to obtain quantitative iodine measurements in digital breast tomosynthesis.

Methods: Contrast-enhanced mammography has shown promise as a cost-effective alternative to magnetic resonance imaging for imaging breast cancer, especially in dense breasts. However, one limitation is the poor quantification of iodine contrast since the true three-dimensional lesion shape cannot be inferred from the two-dimensional (2D) projection. Use of limited angle tomography can potentially overcome this limitation by segmenting the iodine map generated by the first-pass reconstruction using a convolutional neural network, and using this segmentation to restrict the iodine distribution in the second pass of the reconstruction. To evaluate the performance of the algorithms, a set of 2D digital breast phantoms containing targets with varying iodine concentration was used. In each breast phantom, a single simulated lesion with a random size (4 to 8 mm) was placed in a random location within each phantom, with the iodine distribution defined as either homogeneous or rim-enhanced and blood iodine concentration set between 1.4 and 5.6 mg/mL. Limited angle projection data of these phantoms were simulated for wide and narrow angle geometries, and the proposed reconstruction and segmentation algorithms were applied.

Results: The median Dice similarity coefficient of the segmented masks was 0.975 for the wide angle data and 0.926 for the narrow angle data. Using these segmentations during the second reconstruction pass resulted in an improvement in the concentration estimates (mean estimated-to-true concentration ratio, before and after second pass: 48% to 73% for wide angle; 30% to 73% for narrow angle), and a reduction in the coefficient of variation of the estimates (55% to 27% for wide angle; 54% to 35% for narrow angle).

Conclusion: We demonstrate that the proposed two-pass reconstruction can potentially improve accuracy and precision of iodine quantification in contrast-enhanced tomosynthesis. © *2020 The Authors. Medical Physics published by Wiley Periodicals LLC on behalf of American Association of Physicists in Medicine.* [https://doi.org/10.1002/mp.14400]

Key words: breast tomosynthesis, contrast-enhanced imaging, dual energy, quantitative imaging

1. INTRODUCTION

Digital breast tomosynthesis (DBT) is a pseudo-three-dimensional (3D) imaging technique that keeps the high in-plane spatial resolution of digital mammography while adding some vertical resolution that improves visualization of overlapping structures. However, DBT images are still only morphological; the tumor detection is based on differences in attenuation and distortions in the shape of tissues, and therefore are of limited utility after initial diagnosis. Obtaining functional information of the breast would allow for not only an increase in the detection and diagnostic performance of DBT, but more importantly could have a significant impact for postdiagnosis clinical tasks, with several studies indicating that dual-energy contrast-enhanced (DECE) DBT can provide information consistent with dynamic contrast-enhanced magnetic resonance imaging (DCE-MRI).[1–3] However, unlike x-ray tomography where attenuation increases linearly with iodine concentration, the relationship between gadolinium concentration and MRI signal intensity is nonlinear,[4] complicating computation of kinetic parameters. This leads to a potential advantage in using DBT, provided the limitations of the limited angle acquisition can be overcome.

Functional breast imaging is almost exclusively performed by MRI,[5] an accurate but expensive modality, both in terms of equipment and installation costs, and especially in terms of

© 2020 The Authors. Medical Physics published by Wiley Periodicals LLC on behalf of American Association of Physicists in Medicine. This is an open access article under the terms of the Creative Commons Attribution-NonCommercial License, which permits use, distribution and reproduction in any medium, provided the original work is properly cited and is not used for commercial purposes.

operational cost. Other modalities, such as dedicated breast PET and SPECT[6,7] and contrast-enhanced dedicated breast CT,[8] are used to a lesser degree or are still under development, but these also require their own dedicated hardware and, in the case of nuclear medicine applications, extensive radiation protection precautions. In comparison, functional imaging with mammography or DBT would be considerably cheaper and more accessible. However, contrast-enhanced (CE) mammography and DBT lack quantitative capability, making it challenging to accurately and repeatedly measure the functional response of the investigated breast tissue. This is especially important for longitudinal evaluation, such as therapy response monitoring, where it could be important to compare changes in tumor perfusion metrics across several months.

Initial work in contrast-enhanced DBT was based on temporal subtraction,[9] but later the focus moved to dual energy subtraction techniques aiming to avoid patient motion.[10,11] Visual image quality could be improved by optimizing the exposure parameters for dual energy images, including spectrum choice and dose distribution between high and low energy images,[12–14] but to the best of our knowledge, no attempts to improve the quantitative measurements of the visualized iodine maps have been published.

The limitations that need to be overcome for DECE-DBT to become a quantitative modality are demonstrated in Fig. 1, where it is clear that targets with equal iodine content but different sizes and locations within the reconstruction field of view are reconstructed with varying apparent amounts of iodine content. As a consequence of these size- and location-dependent variations, measures such as the slope of the time-enhancement curve, which is indicative of malignancy, cannot be used because of the large influence of lesion size and location on the apparent contrast.

In this work, we propose an approach combining a maximum likelihood-based polychromatic reconstruction algorithm including material decomposition with a deep learning-based segmentation method to allow for better estimation of iodine concentration from limited angle tomography data and demonstrate its effectiveness in simulated data.

2. MATERIALS AND METHODS

The selected approach for our method is to perform a two-pass reconstruction with material decomposition where the iodine component resulting from the first-pass reconstruction is segmented with a deep learning convolutional neural network. This segmentation is then used as a mask in the second pass. We assume that the segmentation problem can be solved in practice due to the expected sparsity of the iodine component. The reconstruction and segmentation methods are described in Sections 2.B and 2.C, respectively. Sections 2.A and 2.D describe the simulation and analysis of a set of phantoms used to evaluate the algorithm.

2.A. Phantom simulation

To evaluate the reconstruction algorithm, we simulated a total of 1124 breast phantom images. To limit the computational cost, the phantoms consisted of 2D coronal slices extracted from a total sample of 50 3D phantoms generated with the algorithm described by Lau et al.[15] An example is shown in Fig. 2. These phantoms were indexed with labels for four different materials: skin, adipose tissue, fibro-glandular tissue, and Cooper's ligaments.

To allow inclusion of background parenchymal enhancement (BPE), the adipose and fibro-glandular components were simulated as mixtures containing 10% and 20% of blood by volume, respectively.[16]

The elemental compositions of these tissues are obtained from the work of Hammerstein et al.,[17] except for the composition of blood, for which values from ICRU report 44[18] were used. These were then used to calculate the energy-dependent attenuation coefficients, $\mu^{(e)}$, using the software from Boone and Chavez.[19] The composition of Cooper's ligaments was assumed to be identical to that of fibro-glandular tissue. The resulting phantoms represented compressed breast thicknesses from 3.0 to 5.6 cm and widths from 5.8 to 18.0 cm with an isotropic voxel size of 0.1 mm×0.1 mm.

The iodinated contrast-enhanced lesions were simulated as ellipsoids and inserted into the generated phantoms. Each background contained a single ellipsoid with a random shape and location within the phantom. Four different groups of lesions were simulated: homogeneously enhanced targets and rim enhanced targets, each split between targets located < 20 mm from the lateral edges and those closer to the middle of the phantom. Except for the criterion of being close or far from the phantom edge, the location of the target was random. Each phantom background was reused for each of the

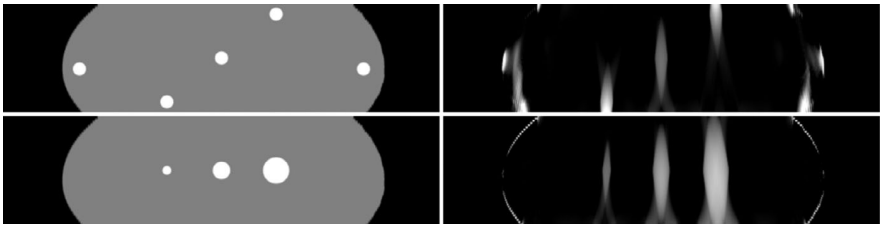

FIG. 1. To demonstrate the absence of quantitative reconstructed attenuation values in limited angle tomography, we simulated a homogeneous phantom composed of fibro-glandular tissue containing lesions of different sizes and a phantom with lesions at different locations, but all with the same iodine concentration. These phantoms are shown on the left side. In the reconstructed iodine maps on the right, it is clear that the reconstructed concentrations depend on both the size of the lesion and the location of the lesion within the reconstructed volume.

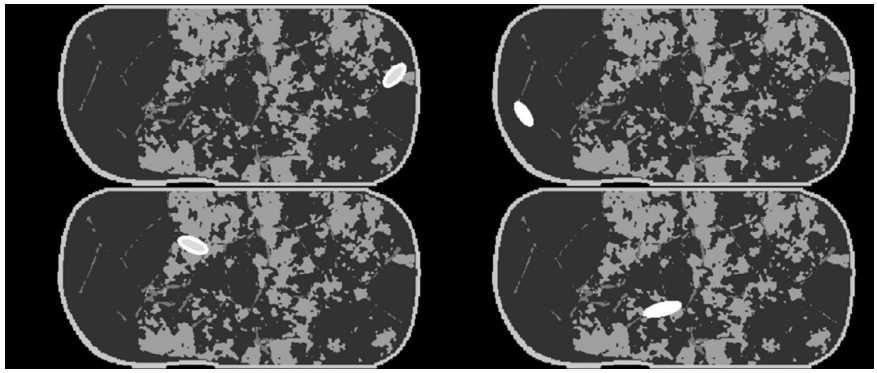

FIG. 2. Four coronal breast phantoms based on the same background structure, each contains the following materials (from darkest gray to white): adipose tissue, Cooper's ligaments, fibro-glandular tissue, skin, and iodine enhanced lesion center and rim.

four groups, resulting in a total of 4496 phantom images. The relative over-representation of targets near the lateral edges was generated because preliminary results had shown that the segmentation of those targets was more difficult and therefore more of those cases were needed to properly train the network performing the segmentation.

The major axis of the lesion varied between 4 and 8 mm, the minor axis varied between 2 mm and the size of the major axis, and rotation was allowed in any direction. Two types of rim enhancement were simulated, 75% of cases had a uniform 1 mm thin rim, and the remaining 25% had a wider rim with thickness equal to half the minor axis.

The lesion composition and its iodine enhancement were based on the values in the work of Kiarashi et al.[16] The target lesions were simulated as a mixture of 60% fibro-glandular tissue and 40% blood by volume. Blood iodine concentration was set at 1.4 mg/mL in the normal adipose and fibro-glandular regions. Within the simulated lesions, blood iodine concentrations were sampled from a uniform distribution of values between 1.4 and 5.6 mg/mL. For the rim-enhanced lesions, concentrations were restricted to between 2.8 and 5.6 mg/mL in the rim, and between 1.4 and 2.8 mg/mL in the lesion center. These blood iodine concentrations correspond to tissue concentration values of 0.16 and 0.28 mg/mL for adipose and fibro-glandular tissues respectively, and values between 0.57 and 2.27 mg/mL for the ellipsoid target regions.

The 2D phantoms were projected onto a one-dimensional detector array by simulating a limited angle fan-beam geometry with the center of rotation placed at the bottom center of the phantom. The x-ray source was placed 650 mm above the center of rotation, and the source-detector distance was 700 mm. Two different angular ranges were investigated, one wide and one narrow. For the wide angle setup, a total of 25 equally spaced projections between $-24°$ and $24°$ were selected, while for the narrow angle setup 15 equally spaced projections between $-7.5°$ and $7.5°$ were used. In both instances, the detector moved together with the source.

The forward model in Eq. (1) was used with a low energy 35 kV tungsten spectrum filtered by 50 μm of rhodium[20] sampled at 0.5 keV intervals, and a high energy 49 kV tungsten spectrum filtered by 1.0 mm of titanium[21] sampled at 1.0 keV intervals. The detector was simulated as a perfect energy integrating detector with pixel pitch of 0.1 mm. No resolution effects, quantum noise, or x-ray scatter were added to the simulated projection data.

2.B. Reconstruction algorithm

We applied a modification of a previously published reconstruction method by Bustamante et al.[22] This method consists of a maximum likelihood method with material decomposition, which features the polychromatic forward model in Eq. (1) and allows decomposition into a set of base materials. All symbols are listed in Table I.

$$\hat{y}_i(\vec{w}) = \sum_e I_0^{(i,e)} \exp\left(-\sum_a \mu_a^{(e)} \sum_j l_{ij} w_{aj}\right) \tag{1}$$

To determine the update step $\Delta\vec{w}$ needed to optimize the log-likelihood cost function $\mathcal{L}$ in Eq. (2), we approximated it with its second order Taylor expansion at the current weights vector $\vec{w}^{(n)}$ and then applied an optimization transfer to a separable quadratic surrogate function for each element w_{aj} of $\vec{w}$. This can be optimized in a single step, shown in Eq. (3), where $\alpha_{aj} \geq 0$ is a design parameter introduced by Fessler et al.[23] This parameter was used to add the information of the segmented iodine image to the

TABLE I. List of symbols.

y_i	Measurement for projection line i
$\hat{y}_i(\vec{w})$	Forward model for projection line i
$I_0^{(i,e)}$	Source spectrum for projection line i
a, b	Indices over the set of base materials
j, k	Indices over the reconstructed voxels
$\mu_a^{(e)}$	Linear attenuation of material a at energy e
l_{ij}	Intersection between projection line i and voxel j
w_{aj}	Weight of material a in voxel j, element of $\vec{w}$
$\mathcal{L}(\vec{w})$	Log-likelihood cost function

reconstruction by setting it equal to 1 inside the segmented target, and equal to 0 outside.

$$\mathcal{L}(\vec{w}) = \sum_i y_i \ln \hat{y}_i - \hat{y}_i \tag{2}$$

$$\begin{aligned} w_{aj}^{(n+1)} &= w_{aj}^{(n)} + \Delta w_{aj}^{(n)} \\ &= w_{aj}^{(n)} + \frac{-\alpha_{aj} \frac{\partial \mathcal{L}}{\partial w_{aj}} |_{\vec{w}=\vec{w}^{(n)}}}{\sum_{bk} \alpha_{bk} \frac{\partial^2 \mathcal{L}}{\partial w_{bk} \partial w_{aj}} |_{\vec{w}=\vec{w}^{(n)}}} \end{aligned} \tag{3}$$

The first derivative in the numerator results in

$$\frac{\partial \mathcal{L}(\vec{w})}{\partial w_{aj}} = \sum_i l_{ij} \left(1 - \frac{y_i}{\hat{y}_i}\right) \psi_i^{(a)}, \tag{4}$$

with

$$\psi_i^{(a)}(\vec{w}) = \sum_e I_0^{(i,e)} \mu_a^{(e)} \exp\left(-\sum_a \mu_a^{(e)} \sum_j l_{ij} w_{aj}\right), \tag{5}$$

and the second derivative in the denominator is

$$\frac{\partial^2 \mathcal{L}(\vec{w})}{\partial w_{bk} \partial w_{aj}} = -\sum_i l_{ij} l_{ik} \left(\frac{y_i}{\hat{y}_i^2} \psi_i^{(a)} \psi_i^{(b)} + (1 - \frac{y_i}{\hat{y}_i}) \psi_i^{(a,b)}\right), \tag{6}$$

with

$$\psi_i^{(a,b)}(\vec{w}) = \sum_e I_0^{(i,e)} \mu_a^{(e)} \mu_b^{(e)} \exp\left(-\sum_a \mu_a^{(e)} \sum_j l_{ij} w_{aj}\right). \tag{7}$$

If we can assume that $\hat{y} \approx y$, which is the case after a good initialization, then the second derivative can be approximated as follows:

$$\frac{\partial^2 \mathcal{L}(\vec{w})}{\partial w_{bk} \partial w_{aj}} \approx -\sum_i l_{ij} l_{ik} \frac{\psi_i^{(a)} \psi_i^{(b)}}{\hat{y}_i}. \tag{8}$$

Putting everything together results in the update step in Eq. (9).

$$\Delta w_{aj}^{(n)} = \frac{\alpha_{aj} \sum_i l_{ij} (\hat{y}_i - y_i) \frac{\psi_i^{(a)}}{\hat{y}_i}}{\sum_i l_{ij} \frac{\psi_i^{(a)}}{\hat{y}_i} \sum_b \psi_i^{(b)} \sum_k l_{ik} \alpha_{bk}} \tag{9}$$

In practice the update steps for each material a and each energy bin e were calculated and applied sequentially, with the loop over the materials within the loop over the energy bins. When using subsets, data from low and high energy spectra were not mixed within a single subset.

We selected adipose tissue, fibro-glandular tissue, and iodine as the three base materials for the reconstruction. To improve convergence, and to push the solution of this underdetermined system towards realistic possibilities, the initial iterations only used two base materials (adipose and fibro-glandular tissue) and included a constraint pushing the sum of the material weight fractions within each voxel towards one. This constraint, shown in Eq. (10), was added as a prior cost function $P(\vec{w})$ with weight $\beta = 10^5$ chosen empirically.

$$P(\vec{w}) = -\frac{\beta}{2} \sum_j \left(1 - \sum_a w_{aj}\right)^2 \tag{10}$$

The iodine component of the reconstruction includes both background and lesion enhancement. In the second pass, only values in the segmented region can be updated, so voxels outside of this region were set to a constant value to account for iodine present outside of the target lesion. This fixed background iodine concentration was set to the median of the pixel values in the first-pass iodine map outside of the segmented lesion and its projection shadow.

The overall two-pass reconstruction workflow, including the segmentation described in Section 2.C, is summarized in the flowchart in Fig. 3.

To further help convergence near the breast edge, the object contour was also used as an additional constraint, as per our previous work.[24,25] In this instance, the free parameter α_{aj} was used as a material specific mask, combining the overall object contour with the material specific segmentation for the iodine component. Including this mask helped to correct the artifacts near the lateral phantom edge seen in Fig. 1. The updated reconstruction with mask is shown in Fig. 4.

The exact phantom contour was used as a binary reconstruction mask $\vec{\alpha}$ for all materials in the first-pass reconstruction, and for the adipose and glandular components in the second pass reconstruction. The segmentation resulting from the method described in Section 2.C was used as mask for the iodine component image in the second pass reconstruction.

Because it is not possible to iterate to convergence for full-sized data, we evaluated the phantom data after a reasonable number of iterations instead of at or near convergence. Therefore, the convergence of the reconstruction was investigated to determine the number of iterations to be used in the experiment.

A random selection of 100 cases was examined for this purpose, checking log-likelihood and proportion of reconstructed iodine up to iteration 100 for the two-material initialization with the prior from Eq. (10), and up to iteration 2000 for the three-material reconstruction. The two-material initialization was performed with 10 subsets (five for each spectrum) and the three-material reconstruction was performed with two subsets (one for each spectrum). A few of the cases were also inspected visually as an extra check on convergence.

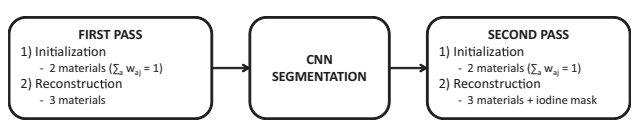

FIG. 3. Reconstruction flowchart.

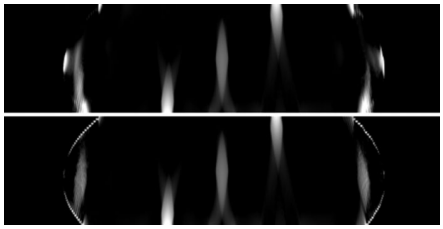

FIG. 4. Continuing the example shown in Fig. 1, the effect of adding the object contour on the iodine component of the reconstruction is shown. In the reconstruction without object contour (left), the targets near the lateral edges now appear near the bottom of the phantom, while they appear in the correct location in the image on the right, after adding the contour information.

2.C. Convolutional neural network based segmentation

The segmentation model was applied locally to each simulated iodine target independently within the complete phantom image. Regions of interest (ROIs) of 256 × 256 pixels (25.6 mm × 25.6 mm) were automatically extracted around each iodine target (both in the first-pass reconstruction of the iodine map and in the original ground truth simulated image). In total, 4400 iodine targets were randomly selected from the set of 4496 cases, and they were split into training (3520, 80%), validation (440, 10%), and evaluation (440, 10%) datasets of the model. The model was a deep learning convolutional neural network (CNN) with modified u-net architecture,[26] detailed in Fig. 5.

The u-net was trained using the simulated iodine-only phantom ROIs as ground truth binary masks. The loss function was composed of two metrics with equal weight into the final loss value: pixel-wise binary cross entropy [BCE, Eq. (11)] and a Dice similarity coefficient [DSC, Eq. (12)]. The training was performed during 200 epochs (the batch size was 10 images) with a starting learning rate of 5×10^{-4}, which was reduced by a factor of 2 if the validation loss did not improve for at least 10 epochs.

$$BCE = \frac{1}{N_{pixels}} \sum_{N=1}^{N_{pixels}} -\mathrm{Truth}_N \times \ln(\mathrm{Model}_N) + (1 - \mathrm{Truth}_N) \times \ln(1 - \mathrm{Model}_N) \tag{11}$$

$$DSC = \frac{2|\mathrm{Mask}^{\mathrm{Model}} \cap \mathrm{Mask}^{\mathrm{Truth}}|}{|\mathrm{Mask}^{\mathrm{Model}}| + |\mathrm{Mask}^{\mathrm{Truth}}|} \tag{12}$$

The trained network was applied to the 440 images in the evaluation dataset, and the resulting segmentation probability map was used to create a binary mask for the iodine component in the second pass reconstruction by setting a threshold at 0.1.

2.D. Data analysis

The accuracy of the segmentation model was evaluated using the Dice similarity coefficient in Eq. (12), which equals 1 for a perfect segmentation and is lower otherwise, with a minimum value of 0. The effects of lesion type (homogeneous vs rim-enhanced), size, orientation, location within the phantom, presence of BPE, and angular range of the acquisition were examined separately.

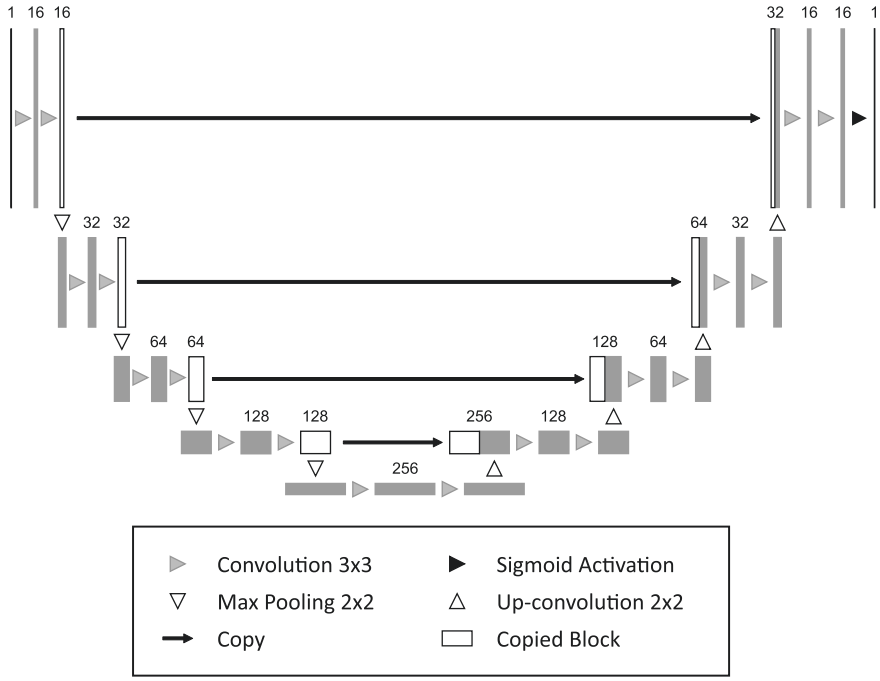

FIG. 5. Schematic overview of the u-net-based architecture[26] used to segment the iodine targets on the reconstructed images. Each 3 × 3 convolution was followed by a batch normalization layer[27] and a leaky rectified linear unit activation layer. The last 1 × 1 convolution was followed by a sigmoid activation layer.

To be able to distinguish between the effects of the segmentation and the reconstruction algorithm, the second pass reconstructions were performed without masking the iodine component, with the CNN-based segmentation, and with the true target segmentation. All evaluations were performed on each of these three method variants and only simulations that included BPE were included in the remainder of the evaluation.

In the reconstruction results, we first evaluated if the detection of rim enhancement was improved when including the segmentation. This was done by calculating the proportion of the reconstructed iodine concentration in the lateral edges (region 1 in Fig. 6) and in the central region (region 2 in Fig. 6). The true rim thickness was used for the rim enhanced targets and a value of 1.0 mm was used for the homogeneous targets. The resulting ROC curves were analyzed using the Dorfman-Berbaum-Metz method for fixed reader and random cases implemented in the RJafroc package.[28] This evaluation was performed for both the wide- and narrow-angle data.

After this, we evaluated the overall accuracy and precision (repeatability) of the method by comparing the median iodine concentration in each lesion with the simulated ground truth. Here we prefer higher precision over higher accuracy, because it is easier to include a calibration factor than to account for large variations between consecutive scans when, for example, following up patients during the course of their treatment. For the reconstructions including the CNN segmentation-based mask and the true target mask, the median concentration was measured within the region determined by their respective masks. For reconstructions without target segmentation, the true target mask was used. The reconstructed iodine fraction was then calculated by dividing the measured median by the ground truth. Data from the wide and narrow-angle simulations were analyzed separately, and sub-analyses were performed evaluating results as function of DSC, iodine concentration, and target size.

For the latter two variables, the reconstructions were split into three groups of approximately equal size for each variable: low (< 1.2 mg/mL), medium (≥ 1.2 mg/mL and < 1.8 mg/mL), and high (≥ 1.8 mg/mL) concentration, and small ($< 40\,\mathrm{mm}^2$), medium ($\geq 40\,\mathrm{mm}^2$ and $< 80\,\mathrm{mm}^2$), and large ($\geq 80\,\mathrm{mm}^2$) sizes.

3. RESULTS

3.A. Convergence

For both the two-material initialization and the three-material reconstruction we found that convergence speed had slowed down after 200 volume updates, corresponding to 20 full iterations for the initialization and 100 full iterations for the reconstruction when taking subsets into account. At this point, the difference between log-likelihood and its maximum was reduced by an order of magnitude. On the other hand, visual inspection of the iodine component images showed little difference after only 10 iterations (20 volume updates). Therefore, the analyses were performed for reconstructions after 10 and 100 iterations, both with a 20-iteration initialization. Because the difference between the reconstructed iodine fraction at these two convergence points turned out to be $< 2\%$, only the results after 10 iterations are presented here.

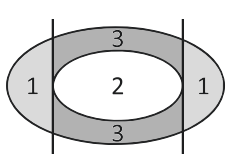

FIG. 6. Measurement regions within an edge-enhanced simulated target.

3.B. Segmentation

The median DSC of the segmented masks in cases with wide and narrow angular range, and with and without BPE, were compared using the Kruskal-Wallis test followed by Dunn's multiple comparison test. Overall, the scores were significantly different, with $P < 0.001$, and all paired comparisons also showed significant differences. In particular, the median DSC [interquartile range (IQR)] in the wide angle case without BPE was 0.980 [0.954–0.991], which was reduced to 0.975 [0.938–0.986] after including BPE ($P = 0.029$). The segmentation results had a lower DSC in the narrow angle case, with median scores of 0.952 [0.900–0.974] and 0.926 [0.849–0.967], before and after including BPE ($P = 0.018$), respectively. These results are also shown in Fig. 7 in the form of an ROC curve formed by placing the DSC values in ascending order. Segmentations of four example cases including BPE are shown in Fig. 8 together with their second pass reconstructions.

In the reconstructions generated from phantoms without BPE, there was no significant difference in the segmentation accuracy between targets that were homogeneously enhanced and those that had rim enhancement, as determined by the Mann-Whitney test. After adding BPE, lesions with edge enhancement were somewhat easier to segment than homogeneous lesions. This trend was significant for the narrow angle case ($P < 0.001$), but not for the wide angle case ($P = 0.062$). The numerical results are listed in Table II.

Spearman correlation coefficients were calculated between the DSC and target iodine concentration, size, location in vertical and horizontal directions (parallel and perpendicular to the line connecting source and detector, respectively), and angle of the major axis of the lesion with the detector plane, in order to gauge the influence of these parameters on the accuracy of the segmentation. Many correlations have significant but small influence on the segmentation quality, but the only factor showing correlations larger than 0.25 is the orientation of the axis of the ellipse, where targets elongated parallel to the detector result in lower DSC than those elongated perpendicular to it. Overall, no correlations larger than 0.5 are found, as can be seen in Table III.

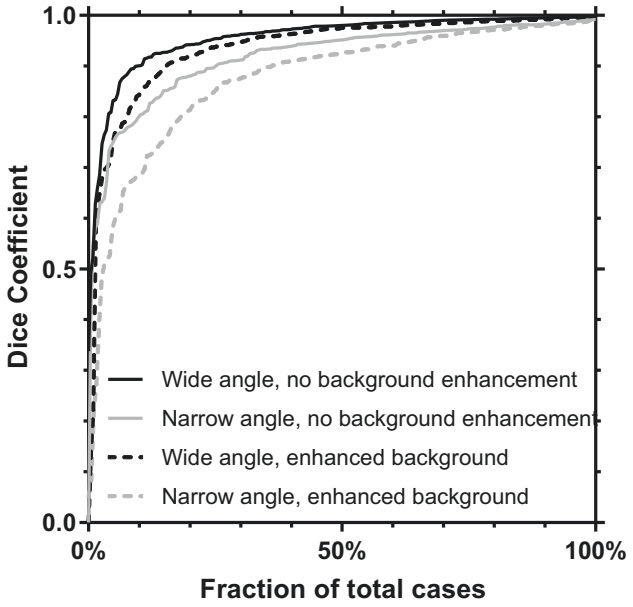

FIG. 7. DSC values placed in ascending order for segmentations from reconstructions of wide and narrow angle projection data, with and without BPE.

3.C. Reconstruction

From this point, only results for simulations that included BPE are shown. The addition of the reconstruction mask was found to improve detection of rim enhancement in the simulated targets. This improvement was significant in both wide and narrow angle cases ($P = 0.022$ and $P < 0.001$, respectively). For the wide angle case, the area under the curve (AUC) [95% CI] improved from 0.915 [0.887–0.943] to 0.934 [0.908–0.960] when adding the segmentation-based mask, and to 0.954 [0.933–0.975] for the ground-truth mask, with only the difference between no mask and the true mask being significant ($P = 0.006$). For the narrow angle case, AUC improved from 0.803 [0.761–0.845] to 0.899 [0.866–0.933] and 0.962 [0.943–0.981], and in this case all differences were significant ($P \leq 0.001$).

The reconstructed iodine proportions of the homogeneously enhanced targets are shown in Fig. 9 for reconstructions without mask, with CNN-based mask, and with the true mask, and means and standard deviations are listed in Table IV. Because the measured proportions were not normally distributed, differences in group means and coefficients

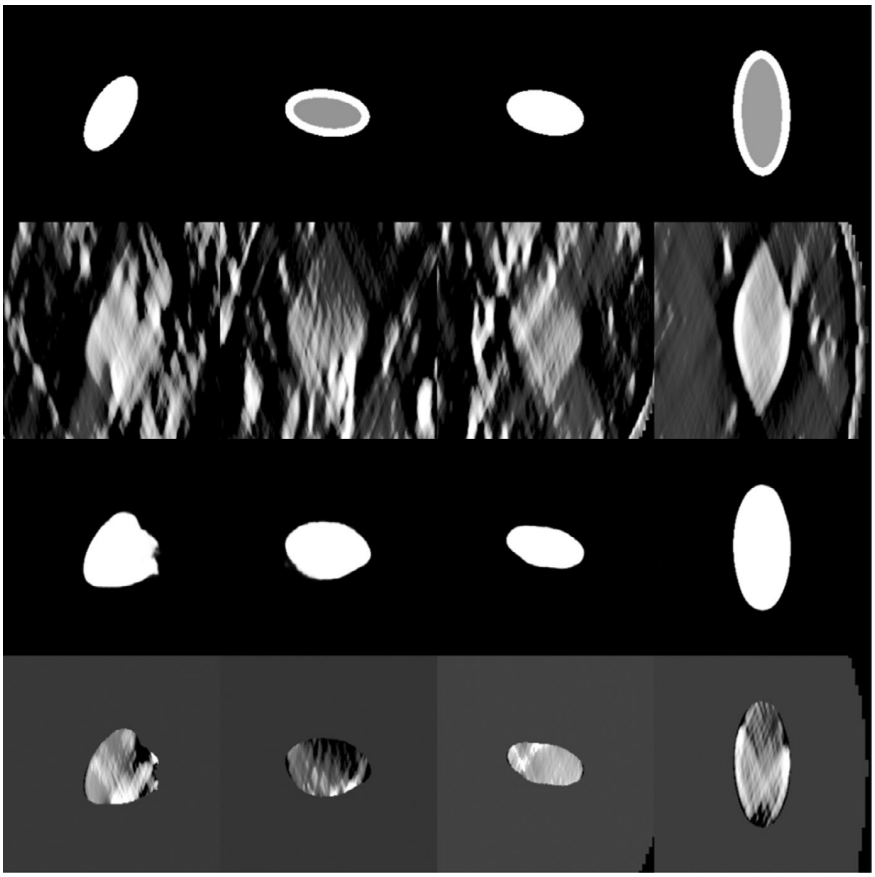

FIG. 8. Four example segmentation and reconstruction results for the wide angle case, showing ground truth on the top row, iodine component of the first-pass reconstruction in the second row, CNN-based segmentation on the third row, and iodine component of the second pass reconstruction on the bottom row. From left to right, the Dice scores are 0.767, 0.910, 0.956, and 0.995, representing the 4th, 15th, 30th, and 95th percentiles of the scores.

TABLE II. Comparison between median DSC and IQR of homogeneous and edge-enhanced cases, with and without BPE, and for wide and narrow angle simulations. P-values were calculated using the Mann-Whitney test.

	Without BPE			Including BPE		
	Median [IQR]		*P*-value	Median [IQR]		*P*-value
Target enhancement	Homogeneous	Rim-enhanced		Homogeneous	Rim-enhanced	
Wide angle	0.980 [0.954–0.991]	0.980 [0.953–0.991]	0.967	0.975 [0.937–0.986]	0.978 [0.952–0.989]	0.062
Narrow angle	0.952 [0.898–0.974]	0.948 [0.888–0.969]	0.195	0.926 [0.849–0.967]	0.955 [0.907–0.977]	< 0.001

TABLE III. Spearman correlation coefficients between DSC and listed parameters.

	Without BPE		Including BPE	
	Wide angle	Narrow angle	Wide Angle	Narrow angle
Iodine concentration	0.22*	0.13	0.20*	0.11
Target size	0.13*	0.23*	0.18*	0.14*
Axis orientation	0.34*	0.26*	0.42*	0.25*
Horizontal position	0.15*	0.02	0.13*	0.18*
Vertical position	−0.01	−0.05	−0.01	0.03

Values marked with * are significant ($P < 0.05$).

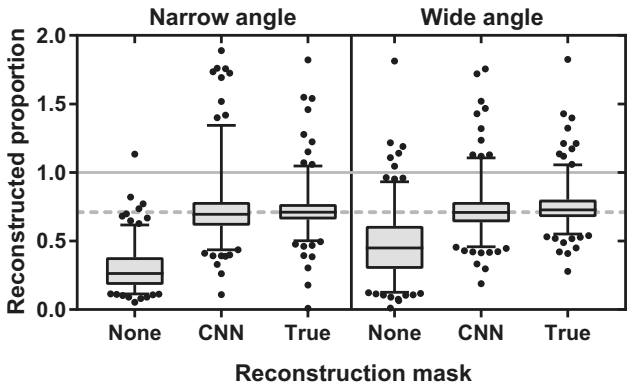

FIG. 9. Retrieved iodine proportions from different reconstruction masks for narrow and wide angle simulations. The boxplot lines are at the 25th, 50th, and 75th percentiles, and the whiskers are at the 2.5th and 97.5th percentiles.

TABLE IV. Mean, standard deviation, and coefficient of variation (CV) of the reconstructed iodine proportions for the different masks and angular ranges.

	Narrow angle			Wide angle		
	Mean	St. Dev.	CV	Mean	St. Dev.	CV
No mask	0.300	0.162	54%	0.476	0.262	55%
CNN mask	0.734	0.257	35%	0.729	0.197	27%
True mask	0.736	0.191	26%	0.756	0.166	22%

of variation (CV) were determined by bootstrapping the data. Measured data were resampled with replacement 1000 times, and mean and CV were calculated for each sample. These bootstrapped distributions approximated the normal distribution so that significance in group differences could be determined by ANOVA followed by Tukey's multiple comparisons test. This procedure was also used for all remaining comparisons in this section. Means and CV were compared for reconstructions without mask, with CNN-based mask, and with the true mask, and this was done separately for the narrow and wide angle simulations. The choice of mask was found to have a significant effect in both cases and on both mean and CV, with $P < 0.001$ in each instance. Further comparison showed that the differences were significant between all groups ($P < 0.001$), except between the CNN-based mask and the true mask for the narrow angle simulation ($P = 0.062$).

Correlations between the reconstructed iodine proportion using the CNN-based masks and segmentation DSC, target iodine concentration, and target size were examined and can be seen in Figs. 10,11, and 12. Spearman correlations are listed in Table V. It should be noted that correlations between iodine proportion and simulated iodine concentration were −0.014 ($P = 0.849$) and −0.020 ($P = 0.776$) when using the true mask instead of the CNN-based mask.

To further examine correlations with iodine concentration and target size, reconstructions using the true lesion mask were split into three groups of approximately equal size for each variable. These results are shown in Figs. 13 and 1, and means and coefficients of variation within each group, again determined via bootstrapping, are listed in Tables VI and VII.

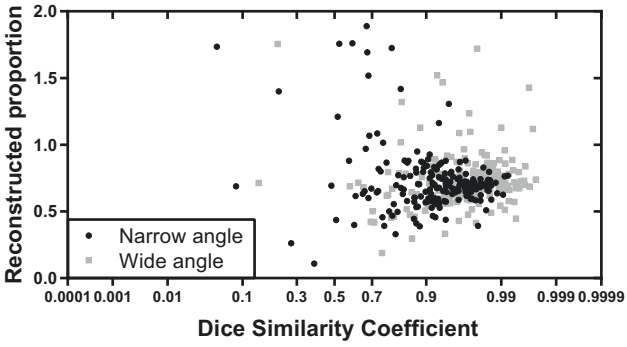

FIG. 10. Retrieved iodine proportion as a function of the Dice similarity coefficient for reconstruction with the CNN-based mask.

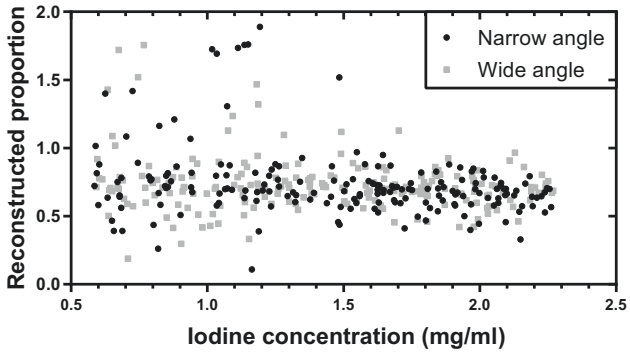

FIG. 11. Retrieved iodine proportion as a function of the simulated iodine concentration for reconstruction with the CNN-based mask.

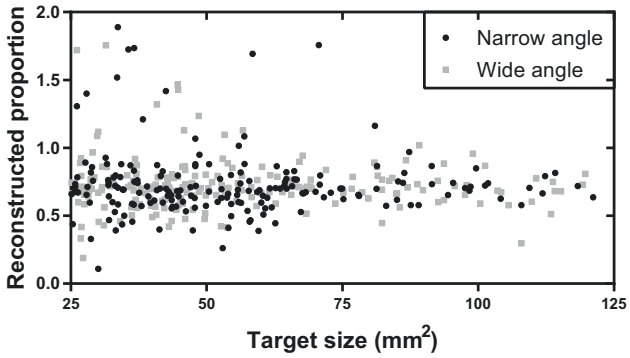

FIG. 12. Retrieved iodine proportion as a function of the simulated lesion size for reconstruction with the CNN-based mask.

TABLE V. Spearman correlation coefficients between reconstructed iodine proportion and listed parameters.

Reconstructed proportion vs	Narrow angle Spearman r	Wide angle Spearman r
Dice similarity coefficient	−0.056	0.208*
Iodine concentration	−0.243*	0.111
Target size	0.021	0.030

Values marked with * are significant ($P < 0.05$)

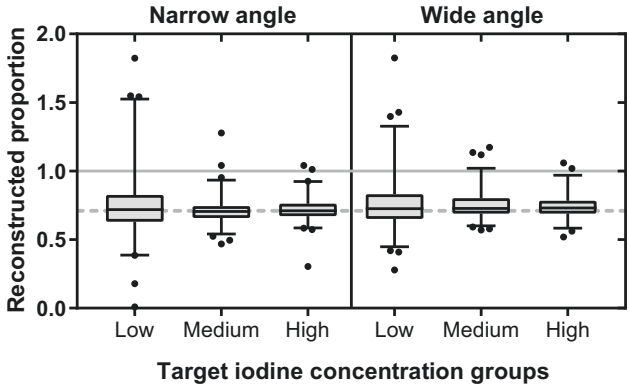

FIG. 13. Retrieved iodine proportions from different iodine concentration groups for reconstructions from narrow and wide angle simulations using the true target mask. The boxplot lines are at the 25th, 50th, and 75th percentiles, and the whiskers are at the 2.5th and 97.5th percentiles.

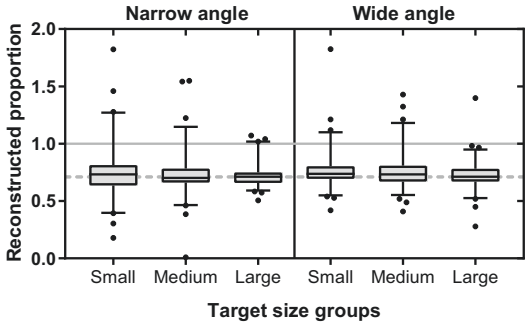

FIG. 14. Retrieved iodine proportions from different target size groups for reconstructions from narrow and wide angle simulations using the true target mask. The boxplot lines are at the 25th, 50th, and 75th percentiles, and the whiskers are at the 2.5th and 97.5th percentiles.

TABLE VI. Mean, standard deviation, and coefficient of variation of the reconstructed iodine proportions for the different iodine concentration groups and angular ranges.

	Narrow angle		Wide angle	
	Mean	St.Dev. (CV)	Mean	St.Dev. (CV)
Low	0.771	0.285 (37%)	0.768	0.230 (30%)
Medium	0.715	0.114 (16%)	0.754	0.113 (15%)
High	0.723	0.108 (15%)	0.742	0.096 (13%)

TABLE VII. Mean, standard deviation, and coefficient of variation of the reconstructed iodine proportions for the different target size groups and angular ranges.

	Narrow angle		Wide Angle	
	Mean	St. Dev. (CV)	Mean	St. Dev. (CV)
Small	0.757	0.242 (32%)	0.770	0.177 (23%)
Medium	0.729	0.204 (28%)	0.771	0.170 (22%)
High	0.724	0.101 (14%)	0.728	0.138 (19%)

The three groups for each variable were compared separately for narrow and wide angle simulations using ANOVA followed by Tukey's multiple comparisons test. The simulated iodine concentration was found to have a significant effect on the mean reconstructed iodine proportion ($P < 0.001$) and its coefficient of variation ($P < 0.001$), and all individual comparisons were found to be significant as well ($P < 0.001$ for all). The same results were found for the effect of the target size, with only the difference between CV of small and medium sized targets in the wide angle case having a slightly larger P-value of 0.012.

4. DISCUSSION AND CONCLUSION

The presented simulation results show that including the CNN segmentation of the iodine region to constrain the reconstruction improved quantification of iodine content,